Nanoscale Advances

ROYAL SOCIETY OF CHEMISTRY

PAPER

View Article Online
View Journal | View Issue

Cite this: *Nanoscale Adv.*, 2025, **7**, 7780

Automated morphological classification and quantification of cerebrospinal fluid extracellular vesicles *via* AFM and machine learning

Mario Kurtjak,†[a] Vera Tomas, †[b] Leon Ivović,[c] David Fabijan, [a] Marko Perčić,[cd] Hrvoje Križan, [e] Marin Tota,[e] Lara Saftić Martinović,[fg] Janja Tarčuković, [bh] Ivan Štajduhar *[c] and Mladenka Malenica *[e]

Morphology of extracellular vesicles (EVs) from cerebrospinal fluid is an important property that could uncover brain-related conditions. However, native morphology could get distorted during imaging, such as with atomic force microscopy (AFM) in air, which enables relatively simple visualisation and automated morphology assessment. Therefore, we compared 24 different preparation methods for the same sample of EVs according to the resulting size, height, aspect ratio and shape distributions obtained from the AFM images. We defined 5 different shape categories (round, flat, concave, single-lobed, and multilobed) and neglected other features that did not fit in either category and were considered artefacts. Artefacts affected the morphometric data (size, height, aspect ratio ranges and distributions), so their neglection was necessary for accurate morphometry. As this required a cumbersome and time-consuming manual search through all AFM images, we developed a computer program that facilitates the individual observation of each particle, enables manual shape identification and exports the resulting size and shape distribution from each AFM image. Since manual EV categorisation in the program still required significant time and proved to be quite subjective, we also employed machine learning for vesicle and shape recognition. A convolution neural network model was trained on a dataset of particles, for which 4 independent researchers provided consistent shape categorisations (F_1 score of 85 ± 5%) and was successfully used to compare the 24 methods of preparation. Our analysis indicated that fixation had a very important role in both capturing and protection of EVs on a mica-based substrate, while critical point drying performed much better in retaining their morphology than hexamethyldisilazane. All tested functionalisations enabled good capture and visualisation of EVs, but (3-aminopropyl)triethoxysilane could cause flattening of EVs and $NiCl_2$ was more prone to formation of round artefacts during direct air-drying. Generally, ethanol gradient dehydration followed by critical point drying best preserved the EV morphology, while chemical dehydration with dimethoxypropane resulted in well-balanced shape distributions with lower aspect ratios. The highest aspect ratios were obtained by ethanol dehydration and critical point drying on $NiCl_2$-coated mica, for which all morphometric data agreed very well with the near-native EV morphology observed in liquid AFM images on the same type of substrate. These findings represent a promising first step towards utilising AFM images of EVs for diagnostic purposes.

Received 8th July 2025
Accepted 24th September 2025

DOI: 10.1039/d5na00665a

rsc.li/nanoscale-advances

[a]*Advanced Materials Department, Jožef Stefan Institute, SI-1000 Ljubljana, Slovenia*

[b]*Department of Anaesthesiology, Intensive Care and Pain Medicine, Clinical Hospital Centre Rijeka, HR-51000 Rijeka, Croatia*

[c]*Faculty of Engineering, University of Rijeka, HR-51000 Rijeka, Croatia. E-mail: ivan.stajduhar@uniri.hr*

[d]*Centre for Micro- and Nanosciences and Technologies, University of Rijeka, HR-51000 Rijeka, Croatia*

[e]*Department of Medical Chemistry, Biochemistry and Clinical Chemistry, Faculty of Medicine, University of Rijeka, HR-51000 Rijeka, Croatia. E-mail: mladenka.malenica@uniri.hr*

[f]*Department of Medical Biology and Genetics, Faculty of Medicine, University of Rijeka, HR-51000 Rijeka, Croatia*

[g]*Faculty of Biotechnology and Drug Development, University of Rijeka, HR-51000 Rijeka, Croatia*

[h]*Department of Anaesthesiology, Resuscitation, Emergency and Intensive Care Medicine, Faculty of Medicine, University of Rijeka, HR-51000 Rijeka, Croatia*

† M. Kurtjak and V. Tomas contributed equally to this work.

1. Introduction

Extracellular vesicles (EVs) are membranous biological nanostructures that contain proteins, lipids, carbohydrates, nucleic acids and even mitochondria in their lumen (without a functional nucleus) with different lipids and proteins, including glycoproteins, tetraspanins and surface receptors, in the phospholipid bilayer.[1] They are formed either by the endocytic pathway or by direct budding from the membrane, resulting in three populations: apoptotic EVs (released by fragmentation of cells undergoing apoptosis), ectosomes/microvesicles formed by outward budding of the plasma membrane and exosomes (released through endocytic pathways from multivesicular endosomes by fusion with the plasma membrane). Furthermore, EVs undergo topological transitions and can be internalised through surface binding, membrane fusion, phagocytosis, macropinocytosis, and clathrin-, caveolae-, and adsorptive-mediated endocytosis.[2,3] This leads to significant heterogeneity in size, morphology, and biochemical cargo. EVs are cell source-specific and can participate in several important events: (i) intercellular communications in normal biological processes, *e.g.*, cell death,[4] and in pathologies; (ii) signalling; and (iii) bidirectional transport of therapeutic agents/bioactive molecules across the blood–brain barrier.[5,6] Unfortunately, most of these mechanisms remain poorly understood.[2] Due to the presence of EVs in biofluids, they could enable a tissue-free biopsy with minimally invasive disease monitoring and diagnosis.[7] If a clear connection between current EV populations in a biofluid and a pathophysiological condition is discovered, EVs will become reliable biomarkers for early disease detection and prevention. EVs from cerebrospinal fluid (CSF) could be used as biomarkers of certain neurological diseases.[8–11] However, the diagnostic potential of EVs remains untapped as their effective isolation and separation from other biological nanoparticles, such as lipoproteins, as well as their reliable identification, are still challenging.[1,6]

The International Society of Extracellular Vesicles (ISEV) recommends protein content-based EV identification and distinction from contaminants after isolation,[12,13] electron microscopy (EM) and atomic force microscopy (AFM) for assessing their morphological properties.[14] EM has traditionally been employed for morphology investigations. However, in the last decade, there has been a growing interest in the application of AFM, which emerged as a valuable technique for measuring three-dimensional (3D) topography and morphology, size distribution, and biomechanical properties of nano-sized samples.[14–17] This method operates by exploiting the interaction between the tip of a cantilever and the sample surface, enabling generation of a three-dimensional image of the sample surface. To preserve the soft and fragile structure of EVs, the dynamic, tapping (oscillating) mode is preferred for imaging. Before imaging, isolated EVs are adhered to a relatively flat surface using electrostatic interactions, chemical bonds, physical adsorption, hydrophobic interactions, or other methods.[18] However, the same electrostatic forces that immobilise the EVs to the surface can also distort their shape, which makes post-imaging data analysis essential.[19] Grains or particles protruding out of the flat substrate, which should predominantly represent EVs in a well-isolated sample, can be readily identified from AFM images. Subsequently, their volume, size, area, and other morphometrics, such as the average aspect (height/radius or height/diameter) ratio,[20] can be calculated and displayed automatically, but such analysis does not provide information regarding their shape and topography. Nonetheless, through meticulous manual examination of each grain across multiple AFM images obtained in a liquid environment, we recently identified various 3D shapes of EVs from CSF in their near-native state (round, flat, single-lobed, multilobed, elongated bulging, concave and partially open). These findings may correlate with various internal morphologies previously observed by cryo-TEM.[21,22]

Here we continue this investigation by visualisation of dried samples by conventional and more attainable AFM in air, which is faster and easier to use (thus more appropriate for inexperienced users) and also enables batch processing of multiple samples.[18] This approach presents two primary challenges: (i) sample preparation, primarily involving the entrapment of EVs on a substrate and preservation of their 3D morphology during the drying process; (ii) the slow, lengthy and subjective determination of EV shape distribution. We are addressing these challenges by comparing different mica functionalisations for attachment of EVs, various dehydration and drying methods, and by automation of the morphometry analysis and shape classification from the obtained AFM images. We developed a computer program for faster individual particle/grain presentation and easier shape classification and then applied machine learning (ML) for EV shape recognition. ML can interpret, classify, and identify patterns in the complex and heterogeneous data, which could improve medical diagnostics based on liquid biopsy platforms and nanostructure-based optical readouts.[23] Applying ML in time-resolved fluorescence correlation spectroscopy,[24] Raman spectroscopy,[25] or total internal reflection fluorescence profiling of micro ribonucleic acids from EVs has already helped identify various samples of cancer origin.[26,27] Moreover, a combination of ML and principal component analysis was used for evaluation of the dynamic morphological features of exosomes *via* cryo-TEM-imaging.[28] There have been only a few attempts to apply convolutional neural network (CNN) ML on AFM images of biological cells[16,29] but here we show for the first time the use of CNNs to differentiate and classify EVs from AFM images into one of five possible morphology categories. A variety of approaches, methods, models, and datasets were evaluated, with future perspectives outlined.

2. Materials and methods

2.1. Cerebrospinal fluid

The sample used in this study consisted of chromatographically isolated EVs from human CSF after a traumatic brain injury (TBI). Collection was conducted under aseptic conditions, in accordance with hospital protocols in the intensive care unit at the General Hospital (Pula, Croatia), utilising ventriculostomy as part of therapeutic intervention for intracranial pressure

monitoring and management. A pool of CSF from four patients (three male patients aged 24, 68 and 73, and one female, aged 71), all with no known comorbidities, was created, collected and stored at −80 °C. All experiments were approved by the Ethics Committee of Pula General Hospital (number: 4943/10-1, 17 July 2019). Informed consent was obtained from a family member for all TBI patients.

2.2. Extracellular vesicles from cerebrospinal fluid

Following a previously published protocol,[22] 5 mL of pooled CSF samples was loaded onto a gravity-driven size-exclusion chromatography (SEC) column (1.5 × 50 cm) equipped with a flow adaptor and a 30 μm bottom frit (Bio-Rad Laboratories, Hercules, CA, USA). The stationary phase consisted of Sepharose CL-6B (GE Healthcare, Danderyd, Sweden), and the mobile phase was phosphate-buffered saline (PBS; Gibco, Thermo Fisher Scientific, Waltham, MA, USA). The column was initially washed with distilled water and equilibrated with PBS. Subsequently, 35 fractions of 2 mL each were collected in low-protein-binding tubes (Eppendorf, Hamburg, Germany) following the initial 5 mL void volume.

For western blot analysis, 48 μL of the pooled CSF and EV fractions were boiled at 95 °C for 10 minutes with the addition of 5× Laemmli buffer (1 M Tris–HCl pH 6.8, 50% glycerol [v/v], 20% SDS [w/v], 1% bromophenol blue [w/v], and 2-mercaptoethanol) and then electrophoresed on 15% SDS polyacrylamide gel electrophoresis (SDS-PAGE, Bio-Rad) using first running buffer (25 mM Tris, 192 mM glycine, and 0.1% SDS, pH 8.3) at 90–150 V. Proteins were transferred to a 0.45 μm PVDF membrane (Merck Millipore Ltd, Tullagreen, Carrigtwohill, Co. Cork, Ireland) at a constant voltage of 17 V for 1 h. The membranes were then blocked with 5% milk in TBS-T (Tris-buffer saline supplemented with 0.1% Tween 20) for 60 minutes and incubated overnight at 4 °C on a shaker with rabbit monoclonal antibodies against CD9 (D8O1A, #13174) diluted 1 : 200 and albumin (#4929) diluted 1 : 3000. Membranes were washed three times for 10 minutes in TBS-T and incubated for 60 minutes with a secondary anti-rabbit IgG horseradish peroxidase-linked antibody diluted in 5% bovine serum albumin blocking buffer (#7074) 1 : 500 for CD9 and 1 : 1000 for albumin. After additional washes in TBS-T, the signal was visualized using SignalFire Elite ECL Reagent (#12757, Cell Signaling Technology, Danvers, MA, USA) and imaged with a laser imager (LI-COR Biosciences, Lincoln, NE, USA).

Following the identification of CD9-positive fractions (5–7), additional analyses were conducted on CSF and pooled EV fractions 5, 6 and 7 with rabbit monoclonal antibodies against CD81 (E2K9V, #52892), TSG101 (E6V1X, #72312), and mouse monoclonal antibodies against Alix (3A9, #2171) diluted 1 : 200, and ApoA1 (5F4, #3350) diluted 1 : 1000. After overnight incubation, previously mentioned secondary anti-rabbit, as well as anti-mouse IgG (#7076) horseradish peroxidase-linked antibodies in 5% bovine serum albumin were applied in the same manner at a concentration of 1 : 500. The images were obtained using the same technique. All antibodies were purchased from Cell Signaling Technology.

2.3. Dynamic light scattering (DLS) and zeta potential

The measurements were conducted using a ZetaPALS instrument (Brookhaven Instruments, NY, USA). Prior to analysis, the samples were diluted 1 : 1 in filtered phosphate-buffered saline (PBS) to achieve the appropriate concentration for DLS (particle size) and phase analysis light scattering (zeta potential) measurements.

2.4. Preparation of EVs for visualisation by AFM

2.4.1 Mica functionalisation. Mica grade V-1, 12 mm in diameter and 0.15 mm thick (Structure Probe, Inc., West Chester, PA, USA) was freshly cleaved, and functionalised by using filtrated (Chromafil RC-20/15, 0.2 μm, 15 mm, Macherey-Nagel, Deutschland) $NiCl_2$, α-poly-L-lysine (PLL) or (3-aminopropyl)triethoxysilane (APTES) as follows. A freshly prepared 50 μL, 10 mM solution of $NiCl_2$ (Sigma-Aldrich, St. Louis, MO, USA) was added on mica, left for 5 min at room temperature, washed 3 times with water (HiPerSolv CHROMANORM, HPLC-grade, BDH Prolabo, UK) and dried under nitrogen flow.[19] For PLL (Sigma Aldrich, UK), 50 μL of 0.001% solution was added to the mica, incubated for 30 min and washed 3 times with ultrapure water. For APTES liquid deposition (APTES-l), 100 μL of a 0.02% APTES aqueous solution was applied to the mica and incubated for 3 minutes in a moist chamber, and then washed 3 times with ultrapure water and phosphate buffer. The sample was immediately added and further processed.[30] For APTES vapor deposition (APTES-v), a mixture of 30 μL of 0.02% APTES and 10 μL of 99.6% triethylamine (VWR International, PA, USA) was dropped onto a Petri dish and placed beneath the hood of an empty desiccator that was flushed with nitrogen. Mica was added inside a Petri dish in the vicinity of the drop and after a 5 minute nitrogen flow, the desiccator was closed and left overnight.[31] For 3D root mean square roughness (Sq, in nm) analysis, fixative droplets (PFA : GA (3% : 1.5%) in PBS) were applied and air-dried on mica and mica substrates functionalised with various methods (prepared in the same manner).

2.4.2 Capture and fixation of EVs on mica substrates. EV-positive eluates after SEC (fractions 5–7) were pooled and equally divided into 24 parts (EV samples). 4 samples (50 μL) were applied onto 4 differently functionalised mica substrates, incubated for 30 minutes at room temperature, and rinsed 3× with PBS and left to directly dry in air, while the remaining 20 samples first underwent fixation in a 1 : 1 ratio with a PBS solution containing 6% paraformaldehyde (PFA, 32% aqueous solution, Electron Microscopy Sciences, Hatfield, PA, USA) and 3% glutaraldehyde (GA, 25% aqueous solution, Spi Chem, West Chester, PA, USA) at room temperature for 10 minutes.[32,33] A 50 μL aliquot of each fixed sample was added to a functionalised mica substrate (5 substrates for each of the 4 functionalisations altogether), incubated for 30 minutes at room temperature and rinsed 3× with PBS and 3× with ultrapure water. 4 samples (each captured on a different kind of functionalised mica) were then dried in air at room temperature, while the other 16 samples were subjected to other more delicate ways of dehydration and drying, as described in the following sections.

2.4.3 Dehydration of extracellular vesicles. Two methods of dehydration were applied: dehydration in an ethanol (EtOH) gradient and dehydration with 2,2-dimethoxypropane (2,2-DMP). EVs were dehydrated with a series of EtOH solutions (99.98%, Gram-Mol d.o.o., Croatia), diluted with ultrapure water (30%, 50%, 70%, 80%, 90%, and 99.98%), leaving the sample for 10 minutes in 1 mL of each dilution in a 12-well plate. Using 2,2-DMP (Alfa Aesar, Germany), the sample was dehydrated in 1 mL of acidified 98% 2,2-DMP (Alfa Aesar, Germany) for 10 minutes at room temperature.[34] Following dehydration, which produced acetone and methanol, the sample was rinsed twice in 100% acetone (Kemika, Croatia).

2.4.4 Drying of extracellular vesicles. After one of the two dehydration methods, each of the 16 remaining undried samples underwent one of the two methods of controlled drying to get 4 possible combinations for each of the 4 different mica functionalisations. For drying with 1,1,1,3,3,3-hexamethyldisilazane (HMDS, GPR RECTAPUR, VWR International, Belgium) in a gradient fashion, the dehydration solution was gradually replaced by HMDS (from 25% to 100%) with 20 minute soaking in-between, and the sample was left to dry overnight in a desiccator after the final solution. For drying at the critical point of CO_2, the sample was placed in a K850 dryer (Quorum Technologies Ltd, UK), and soaked and rinsed three times to completely replace the dehydration solution with liquid CO_2. CO_2 was then eliminated as the supercritical fluid at +35 °C and 86.2 bar within 35 minutes. The dried samples were then stored in a desiccator until AFM imaging.

2.5. Imaging with an atomic force microscope (AFM)

Samples of EVs on mica were imaged using an AFM (Dimension Icon, Bruker, MA, USA) in air tapping mode. The diameter of the cantilever (6.5 nm) had previously been measured using the ImageJ program (Rasband, W.S., U.S. National Institutes of Health, MD, USA) from images of the cantilever (ScanAsyst-Air, Bruker), which were obtained from the Centre for Micro- and Nanosciences and Technologies, University of Rijeka, Croatia, by scanning electron microscopy (JEOL Field Emission JSM-7800F, Japan). The AFM scanning speed was 0.97 Hz, with scanning areas of 10 μm in one direction. Due to the inverse relationship between the amplitude setpoint and the force applied by the tip to the sample, a setpoint amplitude of 150 nm was selected. At this amplitude, the peak force achieved was 214.4 pN, which is considered mild and reduces the risk of sample damage or tip wear. The probe approached the sample at a frequency of 2 kHz. Each sample was imaged at multiple locations, and topographic images were generated. Scanning areas of 1 × 1 μm were captured for calculation of Sq. EVs were also imaged in liquid (PBS) on mica functionalised with $NiCl_2$. 100 μL of sample was placed on mica for 15 min and analyzed using the ScanAsyst (Bruker) probe in liquid in tapping mode.

Topographic images of extracellular vesicles were analysed using Gwyddion 2.6 software (Czech Metrology Institute, Czech Republic) in accordance with the protocol used in the work of Skliar and Chernyshev,[19] but with the modification of skipping the surface reconstruction step (Section S1). A roughness tool was used to evaluate 3D parameters of control surfaces (Sq) as a mean square roughness of height irregularities (otherwise known as the root mean square of height). Further grain analysis applied a height threshold of 20 nm, with additional filtering for a maximum value lower threshold of 20 nm and projected area lower threshold set at 1250 nm^2. Grains touching the edge were excluded from the analysis. Extracted data from Gwyddion included grain centre coordinates (x and y), maximum Martin diameter (max. D), mean height and maximum Z (maximum height, max. H).

2.6. Manual analysis of EV morphology with the help of a custom computer program (EVIAN)

Grain shapes were analysed using a custom-developed Python program, EVIAN (Extracellular Vesicle Image ANalysis),[35] which was utilised for the manual selection of EVs from the grains (by excluding grains that appeared to be artefacts) and for detailed EV shape classification into round, flat, multilobed, single-lobed and concave, or neglecting particles that did not fit these categories. The program reads all measurements (x, y, z coordinates) from the Gwyddion file, as well as grain centres and max. D from the data exported after grain analysis in Gwyddion. Based on these data, the program crops a square frame around each particle with dimensions equal to the max. D and displays the measurements within this frame as a 2D z-map, a 3D rotatable contour, and z-curves in 2D slices through the centre along constant x, y, or both diagonals as well as max. H/max. D. The user can then classify the particle's shape as round, flat, multilobed, single-lobed and concave, or choose to exclude the particle from further analysis. Following each classification, the program partitions the particle data according to the selected shape and provides the corresponding fractions for each category, alongside with EV size, height and aspect ratio range. The program code is included in the SI along with instructions for EVIAN installation and a manual for AFM image processing (Section S1). To ensure reproducibility, classification was independently conducted by four researchers. The dataset used for machine learning comprised all particles from the 24 AFM images that were classified identically by all four researchers.

2.7. Machine learning and automated analysis of EV morphology and statistical analysis

The automated classification of EVs was achieved through a deep convolutional neural network (CNN) model,[36] which was trained on a dataset of 231 unanimously labelled EVs from the 24 AFM images. Prior to model training, some image preprocessing was required. To reduce computational complexity while preserving key morphological features, original images were rescaled to 10 × 10 pixels using bilinear interpolation (upscaling from 5 × 5 to 10 × 10; downscaling from 22 × 22 to 10 × 10; Fig. S1a and b, respectively). In addition, each image was rotated (90°, 180°, and 270°) as well as translated by one pixel in each direction to augment the training data set (Fig. S1c and d, respectively). Next, pixel intensities were normalised between 0 and 1 to reduce the overall variation in the data and

avoid model overfitting. As this leads to loss of the information about the particle aspect ratio, max. H/max. D was introduced as an additional parameter for the training process. The Synthetic Minority Over-sampling TEchnique (SMOTE) was employed for handling relatively small datasets and imbalanced class distribution.[37] Model training was carried out using stratified 5-fold cross-validation, and a grid search was employed to optimize the hyperparameters, including batch size, number of epochs, and choice of optimizer. The dataset was randomly split into five equally sized folds, preserving class distribution. For each fold f, a model was separately trained on the remaining four folds, and then evaluated on the holdout fold f. The process of randomly splitting the data and performing cross validation was repeated ten times, to account for the validation process randomness and to observe model robustness. Thus, we trained and evaluated a total of 50 predictive models independently. The CNN architecture comprised multiple layers: the input layer accepted 10 × 10 single-channel images, followed by a 2D convolutional layer (32 filters, 3 × 3 kernel size, ReLU activation), and a 2 × 2 max pooling layer. This was followed by another convolutional layer (64 filters, 3 × 3 kernel size, ReLU activation) and another max pooling layer. After flattening the output, a dense layer with 64 neurons and ReLU activation was applied, followed by a final softmax output layer corresponding to the six morphological classes. Hyperparameter tuning was performed using a grid search to identify the optimal parameters, such as batch size (10, 32, and 64), number of epochs (50, 100, 150, and 200), and optimizer (Adam, root mean square propagation, and stochastic gradient descent with momentum). The best performing model was selected based on its accuracy and weighted F_1 score during the 5-fold stratified cross-validation process. Performance was evaluated using the weighted F_1 score and the average confusion matrix over the 5-fold cross-validation process. The final model architecture was selected based on the optimal hyperparameters derived from the grid search. After ML, the best performing model performed EV shape recognition and classification on all 567 grains from 24 AFM images (just like all four researchers manually). Additionally, AFM images of EVs for three selected drying methods on $NiCl_2$-coated mica (air drying, ethanol gradient + CPD and DMP + CPD) and liquid AFM on the same substrate were analysed in the same way (two 10 × 10 μm for each, 8 AFM images altogether). Non-parametric Mann–Whitney U was used for comparison of EV max. D, max. H and aspect ratio distributions for these four samples.

3. Results and discussion

3.1. Identification of EVs in SEC eluates

The source of EVs was a pool of CSF collected from patients with TBI using an external ventricular drainage system. EVs were isolated from the pooled CSF (5 mL) by in-house gravity-driven SEC (Fig. 1a). Western blot analysis was then performed on the 35 eluates to confirm the presence of EVs through detection of their transmembrane protein marker CD9 and elimination of contaminants by monitoring the presence of albumin. A strong CD9-positive signal was observed in fractions 5 to 7 and 18 to 22 (Fig. 1b). However, while fractions 5–7 were free of contaminants, the later fractions showed a very strong albumin signal. This phenomenon has been observed previously and is likely due to non-specific CD9-antibody binding to albumin which can act as a binding agent at high concentrations.[22] Consequently, fractions 5 to 7, which showed a strong and specific CD9 signal, were selected to create an EV-enriched pool (6 mL), referred to as the $CD9^+$ EV pool (Fig. 1b, red triangles).

In accordance with the Minimal Information for Studies of Extracellular Vesicles (MISEV) guidelines,[12,13] we further confirmed the presence of EVs in the EV pool using four different EV markers and compared it to the CSF pool (Fig. 1c). CD9 and CD81 were detected in both samples, whereas internal EV markers, such as Alix and TSG101, were weakly expressed in the initial CSF sample but absent in the purified EV fractions. This was further corroborated by the absence of signals for albumin and apolipoprotein A1 (ApoA1), common non-EV contaminants, in the pooled EV fractions (Fig. 1c).

Additionally, size distribution analysis (based on scattering of light) of the pooled EVs revealed a size range from 141.7 to 243.2 nm, with the majority of particles exhibiting hydrodynamic diameter between 140 and 180 nm (Fig. 1d). This size range aligns with the established size of EVs, which typically spans from ∼30 to several hundred nm.[22,38] The zeta potential measurements of the pooled EVs ranged from −34 mV ± 1 mV, indicating a stable colloidal suspension. These values are consistent with previous reports, which suggest that EVs typically exhibit negative zeta potentials due to the presence of negatively charged phospholipids and proteins on their surface.[39]

In summary, the SEC purification method effectively concentrated EVs from the CSF, as evidenced by the lack of common contaminants and the clear presence of EV-specific markers. The isolated vesicles exhibited typical size and zeta potential values associated with biologically active EVs, further confirming the robustness of the isolation procedure.

Previous studies have employed ultracentrifugation for EV isolation, which, although effective, frequently co-isolates non-EV contaminants, such as lipoproteins.[13] By contrast, our use of SEC demonstrated a purer EV population. This finding is consistent with our previous work[40] and with others reporting that SEC reduces protein contamination, thereby improving the quality of downstream analyses.[41,42]

3.2. Sample preparation for AFM and manual analysis of EV morphology

In this study we compared four different functionalisations of mica and six different sample drying methods. First, we examined whether mica functionalisation and the use of fixatives contributed to increased surface roughness. As shown in Fig. S2, the root mean square surface roughness (Sq) increased (up to 1.73 ± 0.05 nm, with features as high as 20 nm, in the case of $NiCl_2$, Fig. S2b) in relation to bare mica (with Sq = 0.28 ± 0.02 nm, Fig. S2a) for all functionalisations except PLL, for which it even slightly decreased (Fig. S2d). These results are consistent with the literature.[43–45] Interestingly, addition of the fixative (PFA : GA; 3% : 1.5%) decreased the Sq for $NiCl_2$ and

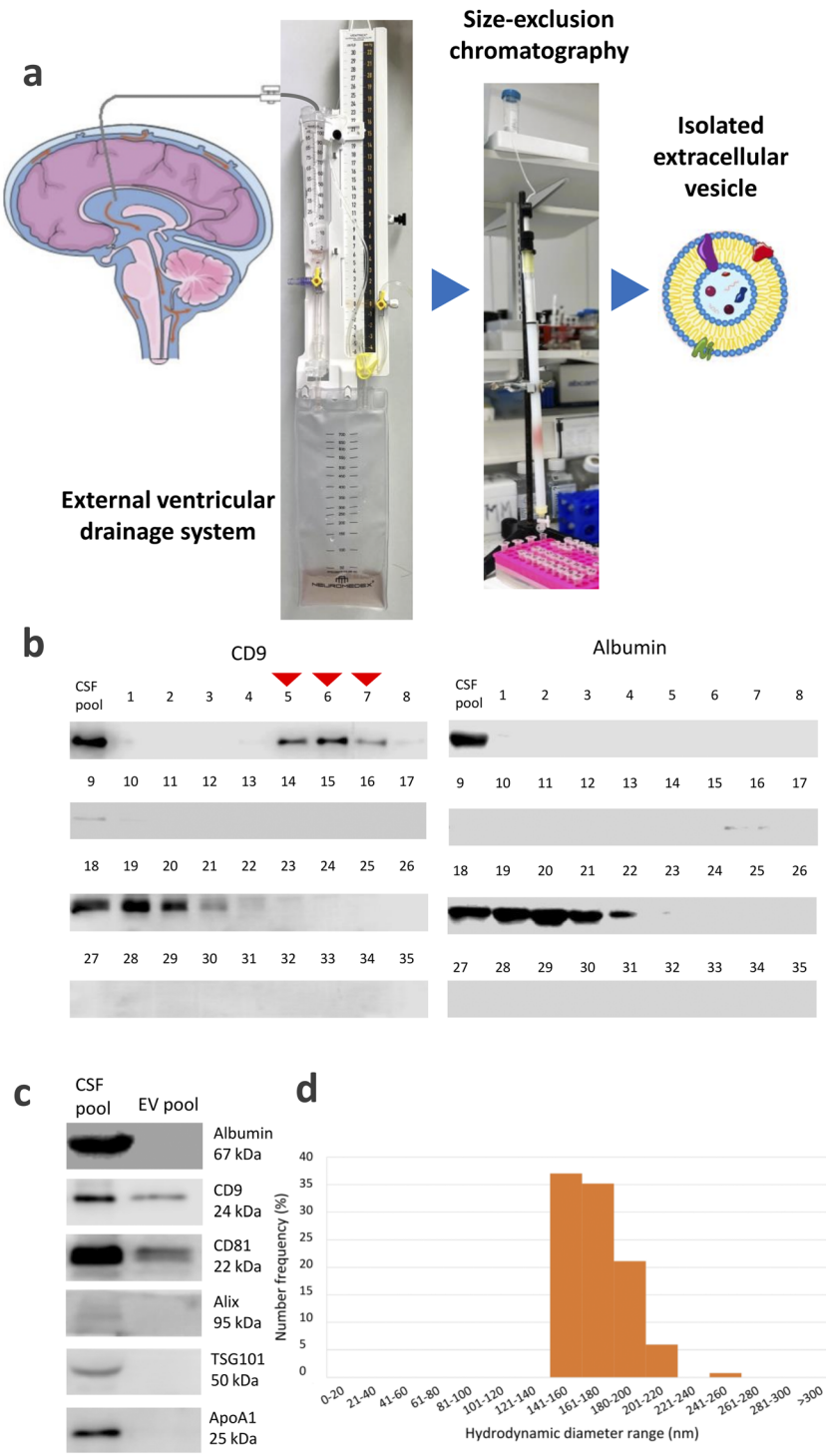

Fig. 1 Isolation of extracellular vesicles from cerebrospinal fluid using size-exclusion chromatography (a), with western blot analysis on CD9 and albumin across fractions (b), protein marker validation of the CSF pool and EV pool (c), and size distribution of particles in the EV pool by dynamic light scattering (d).

APTES-l (Fig. S2c and i), had virtually no effect in the case of APTES-v (Fig. S2g) and increased it for PLL (Fig. S2e). This is most likely due to different $NiCl_2$ crystal growth in the presence of fixatives, conformational changes of lysine chains in the case of PLL and crosslinking of amino groups in APTES with the help of the fixative.[46,47] While the final functionalised surfaces exhibit a similar pattern for PLL, APTES-l and APTES-v, distinct particles in the size range of EVs can be observed in the case of $NiCl_2$. Such artefacts could easily be mistaken for EVs during AFM image analysis.[19] To avoid this as much as possible, we set a threshold of 20 nm for the minimal height when detecting particles/grains from the recorded AFM images.

We applied EVs in PBS (used as a mobile phase in SEC) onto the four types of functionalised mica substrates and dehydrated and dried the samples under different conditions, which yielded altogether 24 distinct preparation protocols and 24 different specimens for observation by AFM (Table 1). 4 samples were directly applied to mica substrates without any prior fixation (marked with – in the second column of Table 1), while the other 20 were dropped onto the substrates only after fixation in a PFA : GA 3% : 1.5% mixture (+ sign in the second column of Table 1). This combination of fixatives was used based on its demonstrated efficacy in preserving mitochondrial morphology.[32] Other fixative compositions from PFA and GA and fixation protocols prior to or after attachment onto the substrate can be encountered in preparations of non-adherent cells, liposomes, bacteria and vesicles for AFM imaging.[18,33,48–51] Hence, there is room for further optimisation of this preparation step, especially when applying immune-based detections.[18]

Although it is known that it can collapse the EV outer structure, simple drying of samples in air is still the preferred method. Here we also included other ways of dehydration and drying (Table 1), which mitigate the damaging effects of osmotic pressure (during washing with pure water to prevent PBS salt crystal growth on the samples) and high water surface tension.[18,52]

Table 1 Extracellular vesicle sample preparation protocols for AFM visualization and grain analysis with the Gwyddion program[a]

No.	Fixation	Functionalisation	Dehydration	Drying
1	—	$NiCl_2$	—	Air
2	—	PLL	—	Air
3	—	APTES-v	—	Air
4	—	APTES-l	—	Air
5	+	$NiCl_2$	—	Air
6	+	PLL	—	Air
7	+	APTES-v	—	Air
8	+	APTES-l	—	Air
9	+	$NiCl_2$	EtOH	CPD
10	+	PLL	EtOH	CPD
11	+	APTES-v	EtOH	CPD
12	+	APTES-l	EtOH	CPD
13	+	$NiCl_2$	DMP	CPD
14	+	PLL	DMP	CPD
15	+	APTES-v	DMP	CPD
16	+	APTES-l	DMP	CPD
17	+	$NiCl_2$	EtOH	HMDS
18	+	PLL	EtOH	HMDS
19	+	APTES-v	EtOH	HMDS
20	+	APTES-l	EtOH	HMDS
21	+	$NiCl_2$	DMP	HMDS
22	+	PLL	DMP	HMDS
23	+	APTES-v	DMP	HMDS
24	+	APTES-l	DMP	HMDS

[a] PLL: poly-L-lysine; APTES-v: (3-aminopropyl)triethoxysilane vapor deposition; APTES-l: (3-aminopropyl)triethoxysilane liquid deposition; EtOH: ethanol; CPD: critical point drying of CO_2; HMDS: hexamethyldisilazane; DMP: 2,2-dimethoxypropane.

Given the large number of preparation protocols and the requirement to image a sufficiently large area to capture an adequate number of EVs for meaningful morphological analysis, combined with the relatively slow imaging speed of AFM,[16] the resolution of AFM images was relatively low. They were 512 × 512 pixels in size and covered 10 μm × 10 μm (100 μm^2) of specimen area, which means that the cantilever scanned in steps of 19.5 nm, so a particle of such diameter would consist of only one pixel. To address this limitation, we selected another filter (in addition to the 20 nm minimal height) that considered ≈20 nm as the minimum radius of a spherical particle that would be detected as a grain in Gwyddion, which set the lower threshold for projected area to 1250 nm^2. Based on these filters, the program automatically detected grains in each of the 24 AFM images and their number, and their sizes expressed as max. *D*, mean heights and max. *H* could be easily exported.

However, to examine each grain morphologically in Gwyddion, it would require significant effort and time. Therefore, we wrote a custom Python program that reads the Gwyddion file, cuts out, zooms and displays each detected grain and enables manual shape categorisation. Hence, we named it EVIAN (Extracellular Vesicle Image ANalysis).

Fig. 2 demonstrates how a vesicle looks like in a 10 × 10 μm image in Gwyddion (indicated with an arrow, Fig. 2a) and then when cropped and displayed in EVIAN (Fig. 2b). The latter displays max. *H*/max. *D* value, and visualises each grain as a 2D map of *Z* values (Fig. 2b(i)), a 3D contour that can be rotated (Fig. 2b(ii)) and as cross-sections in four distinct *Z*-planes (Fig. 2b(iii)).

In our previous investigation of EVs from CSF, we observed and named their various 3D shapes by AFM for the first time.[22] Here we aimed to refine these definitions to enable more distinct and objective counting of the shapes. Based on the analysis of 2D maps, *Z*-profiles, aspect ratios and 3D plots, following the shape models presented in Fig. S3, four investigators classified each particle into one of six shapes: round, concave, single-lobed, multilobed, flat, or neglected. The classification criteria were defined as follows: multilobed particles had at least three peaks of approximately equal height; concave particles had two peaks with a distinct valley; flat particles displayed monotonous *Z*-curves; round particles had a max. *H*/max. *D* ratio ≥0.2; and single-lobed particles had one prominent peak with a height ≥5%. Particles that did not meet these criteria were classified as neglected. Following these guidelines, four independent researchers blindly analysed and classified the grains from all 24 AFM images (altogether 567 grains), which means that they could not relate the images to the 24 preparation methods. Table 2 shows the EV number, size (max. *D*) and max. *H* range of grains for each preparation protocol after analysis in Gwyddion and after analyses in EVIAN.

Considering the number of grains detected in Gwyddion (Table 2), we can eliminate protocols 1–4, which involve only dropping, incubating, washing and drying in air, as they all resulted in a notably lower number of grains, most probably due

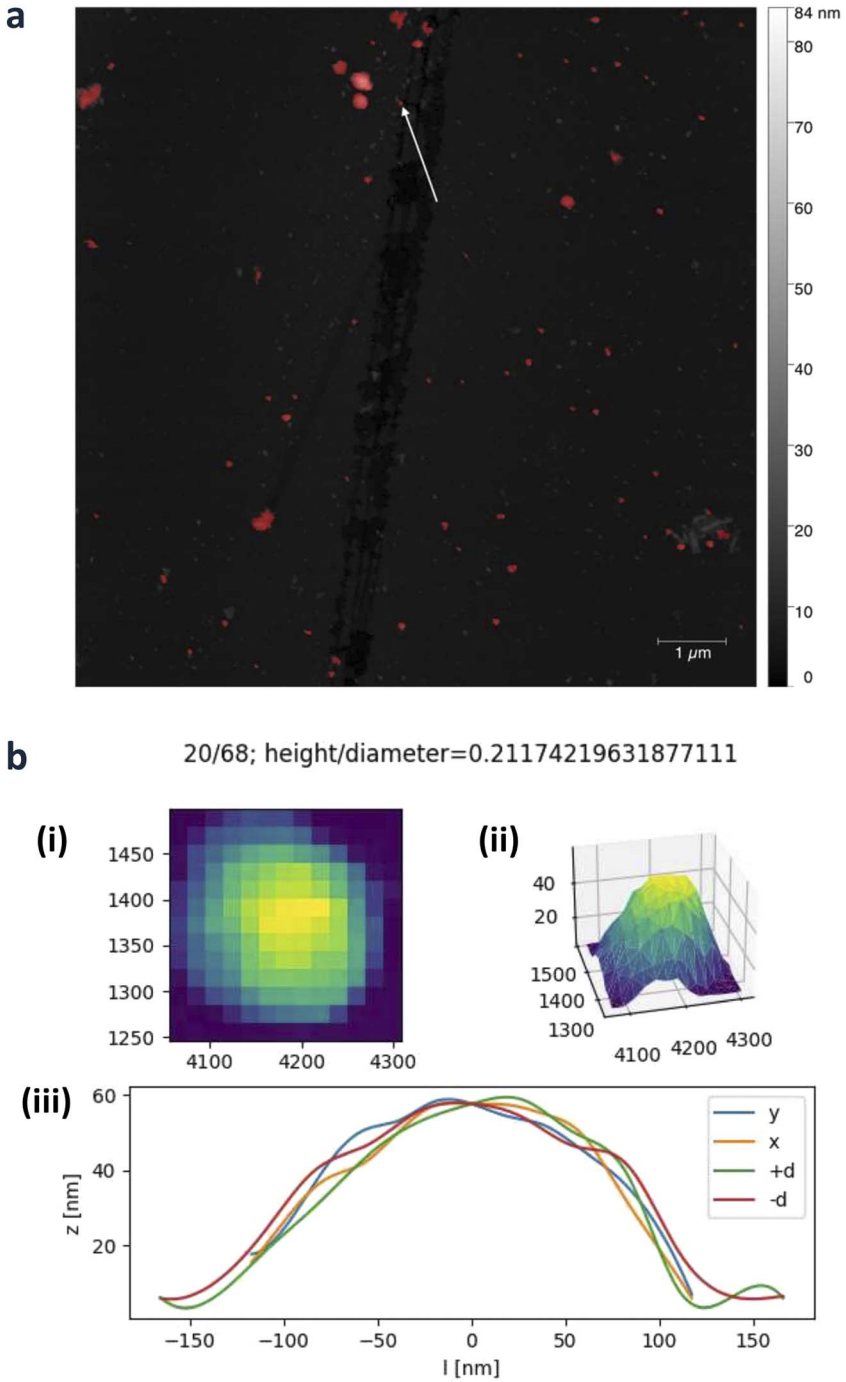

Fig. 2 Atomic Force Microscopy (AFM) analysis of extracellular vesicles (EVs). (a) AFM topography image in Gwyddion showing detected grains (red) and their distribution across the surface. The arrow points to the grain that is displayed individually with the use of EVIAN below (b). The assigned ordinal number (20) of the selected grain and total number of detected grains (68) in the 10 × 10 μm AFM image, as well as the aspect ratio, are shown on top. Underneath the program plots: (b(i)) Heatmap representation of the selected grain (EV), capturing the intensity distribution across the surface area. (b(ii)) 3D surface contour of the EV showing morphological features, such as height variations. (b(iii)) Cross-section of the EV along different axes (*x*, *y*, +*d*, and −*d*), providing detailed height (*z*) values.

to damage of the integrity and structure of EVs during the drying process. By comparing to samples 5–8, which were also air-dried but underwent fixation before dropping onto the mica substrate and drying, we can generally observe an increase in the number of grains, particularly for $NiCl_2$ (5) and APTES-l (8) functionalisation, which provided larger surface roughness (confront Fig. S2) and thus better surface coverage with a functionalising agent. Generally, in the case of $NiCl_2$, the enhanced bonding is due to positively charged mica, while with APTES, the aldehyde groups of yjr fixative bond together the primary

Table 2 Grain analysis of AFM images in Gwyddion and EVIAN on a 100 μm^2 surface showing the total number (*N*), maximum Martin diameter range, and maximum height range

	Gwyddion			EVIAN		
No.	Total *N*	Maximum Martin diameter range (nm)	Maximum height range (nm)	Total *N* range	Maximum Martin diameter range (nm)	Maximum height range (nm)
1	3	80–270	23–60	2–3	84–270	23–60
2	6	60–277	24–45	3–4	85–277	24–45
3	6	67–169	23–51	2–3	101–169	23–51
4	14	56–295	21–79	9–12	102–295	23–79
5	24	123–488	28–99	16–24	123–488	28–99
6	6	63–406	21–65	2–5	82–406	23–65
7	8	123–388	28–66	6–8	123–388	28–66
8	68	56–417	20–81	45–54	75–417	20–84
9	30	56–584	21–121	17–25	77–584	21–121
10	40	56–434	24–104	27–30	75–434	26–104
11	20	70–428	22–88	13–18	70–428	21–88
12	32	56–562	23–77	18–25	75–562	25–77
13	39	56–667	23–87	23–30	67–667	24–87
14	28	56–386	23–52	15–19	79–386	26–52
15	38	56–275	21–48	16–24	82–275	22–48
16	56	56–288	21–44	28–39	70–288	21–44
17	8	85–234	21–61	2–8	85–234	21–61
18	9	60–147	22–48	3–6	67–147	22–48
19	20	60–306	22–93	11–16	80–306	25–93
20	68	60–283	21–38	38–59	75–283	22–38
21	7	67–647	26–75	4–5	94–647	26–75
22	4	63–89	22–29	0–2	80–89	26–29
23	25	56–312	23–84	15–22	80–312	24–84
24	8	67–126	21–34	3–6	70–126	22–34

amino groups of APTES and amino groups on the surface of EVs belonging to membrane proteins or lipids with a phosphatidylethanolamine headgroup.[53] Similarly, the number of detected grains was notably lower after combination of chemical dehydration and drying (DMP + HMDS, preparation methods 21–24), possibly due to some interference of the two chemicals with the mica functionalisation, except in the case of APTES-v functionalisation (23). HMDS did not appear to be effective with $NiCl_2$ and PLL surfaces, even when using an ethanol gradient (samples 17 and 18), while the remaining 10 protocols (9–16, 19 and 20) yielded a sufficient number of particles for analysis. All particle numbers further decreased after morphological classification in EVIAN, during which certain particles were neglected as artefacts (columns in the right half of Table 2). However, we should bear in mind that we assumed here that the variability in particle number is mainly a consequence of strength of their binding to the substrate and preservation of morphology, but it could likely arise also from differences in sample handling, EV heterogeneity within the EV pool and technical limitations during AFM imaging.

The max. *D* of the detected grains ranged from approximately 60 to 600 nm, falling within the typical size range of EVs and well above our selected size threshold, while the max. *H* values ranged from 20 to 120 nm. However, if we compare these values with the values obtained after EV classification in EVIAN, we can see that the range of max. *D* shifted towards larger values (around 70–670 nm) as the lowest sizes increased while the largest stayed the same. This suggests that the majority of artefacts that were neglected during this process were in the smaller size range. Consequently, analysis solely based on Gwyddion grain detection can result in EV size distributions that are inaccurately skewed toward smaller values. Such a shift has been observed before, when the sizes of EVs from CSF were determined by different methods and AFM yielded a smaller mode size.[22] The values adjusted after neglecting artefacts in EVIAN align more closely with the size range (141.7 nm to 243.2 nm) detected by PALS in this investigation. Nevertheless, it is also plausible that, due to low resolution of AFM imaging, smaller grains were more frequently recognised as artefacts. A similar effect was observed for the max. *H* values, although not to the same extent as in the size distributions. Additionally, due to discrete lateral shifts inherent in AFM image acquisition and relatively low resolution, certain max. *D* may be identical across different samples.

The aspect ratio (height/diameter or height/radius) has been considered an important parameter in the previous morphometric investigations of EVs, *e.g.*, for the determination of the relationship between the size, deformation degree, and mechanical properties of EVs from the liquid biopsy of multiple myeloma patients,[54] prediction of the host from three different cancer cells[29] and comparison between tumour-derived and normal cell line EVs.[55] Therefore, we calculated it for each recognised grain in this study as max. *H*/max. *D*. Throughout the 24 sample preparation methods, the particle aspect ratios span from around 0.06 to around 0.7 (Fig. 3), which is in agreement with previous studies.[54] Vorselen *et al.*[17] obtained 0.5–0.75

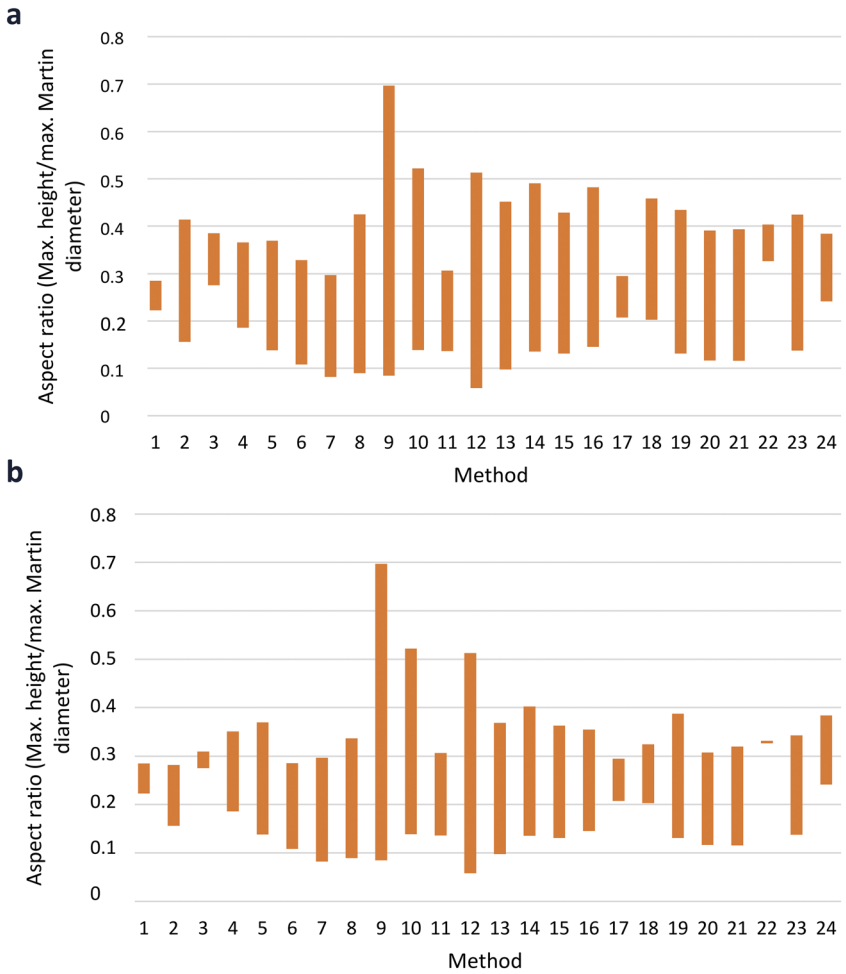

Fig. 3 Morphometry analysis: aspect ratio (maximum height/maximum Martin diameter) ranges for 24 different methods: (a) data after grain analysis in Gwyddion and (b) non-neglected particles after analysis by four investigators using EVIAN. Legend for methods: without fixation + air-dried (1 – $NiCl_2$, 2 – PLL, 3 – APTES-v, 4 – APTES-l); fixed + air-dried (5 – $NiCl_2$, 6 – PLL, 7 – APTES-v, 8 – APTES-l); fixed + EtOH + CPD (9 – $NiCl_2$, 10 – PLL, 11 – APTES-v, 12 – APTES-l); fixed + DMP + CPD (13 – $NiCl_2$, 14 – PLL, 15 – APTES-v, 16 – APTES-l); fixed + EtOH + HMDS (17 – $NiCl_2$, 18 – PLL, 19 – APTES-v, 20 – APTES-l); fixed + DMP + HMDS (21 – $NiCl_2$, 22 – PLL, 23 – APTES-v, 24 – APTES-l).

values for red blood cell EVs from 3 donor samples. Such hemispherical shapes, with H/D values around 0.5, are also typical for liposomes.[20] On the other hand, Yokota *et al.*[56] detected lower aspect ratios (around 0.20 H/D) for tethered EVs from different cell lines (Sk-Br-3 and HEK293) on nanospots of the polyethylene glycol–lipid conjugate in a chip. Comparison of aspect ratio ranges before (Fig. 3a) and after elimination of artefacts in EVIAN (Fig. 3b) reveals notable narrowing towards smaller values for all methods except 1, 4, 5, 7, 9–12, 17 and 24. Methods involving fixation, dehydration in ethanol gradient and CPD (9, 10 and 12) stand out with the widest range of aspect ratios (the only three methods providing aspect ratios above 0.5), with the exception of method 11 (APTES-v functionalisation), which exhibits one of the narrowest and lowest aspect ratio ranges among methods yielding at least 15 EVs/100 μm. On the other hand, method 12 (fixative + ethanol gradient + CPD on APTES-l mica) also yielded the lowest minimum aspect ratio value (around 0.06), which could also be a sign of flattening. This indicates that APTES functionalisation might be responsible for flattening of EVs, presumably due to strong interactions with APTES molecules on the surface of mica.

This is further evidenced in the morphological classification by the four investigators, presented in Fig. 4, with the shape distribution for each preparation method shown in different colours (orange = round, yellow = single-lobed, violet = concave, blue = multilobed, grey = flat, and green = neglected). Variations in classifications among investigators were noted, likely due to subjective interpretation and difficulty in categorizing certain shapes. Nevertheless, we can draw some conclusions by comparing the 12 methods that yielded on average at least 15 EVs/100 μm (5, 8, 9–16, 20 and 23) after elimination of artefacts through EVIAN. Method 20 (APTES applied as liquid solution and EtOH + HMDS gradient drying) stands out with the largest fraction of flat shapes, about which all four investigators agreed. A very evident fraction of flat shapes can also be discerned for method 11 (APTES deposited as vapours and drying through the EtOH gradient and CPD). This is in agreement with the lower aspect ratio that was also characteristic for both

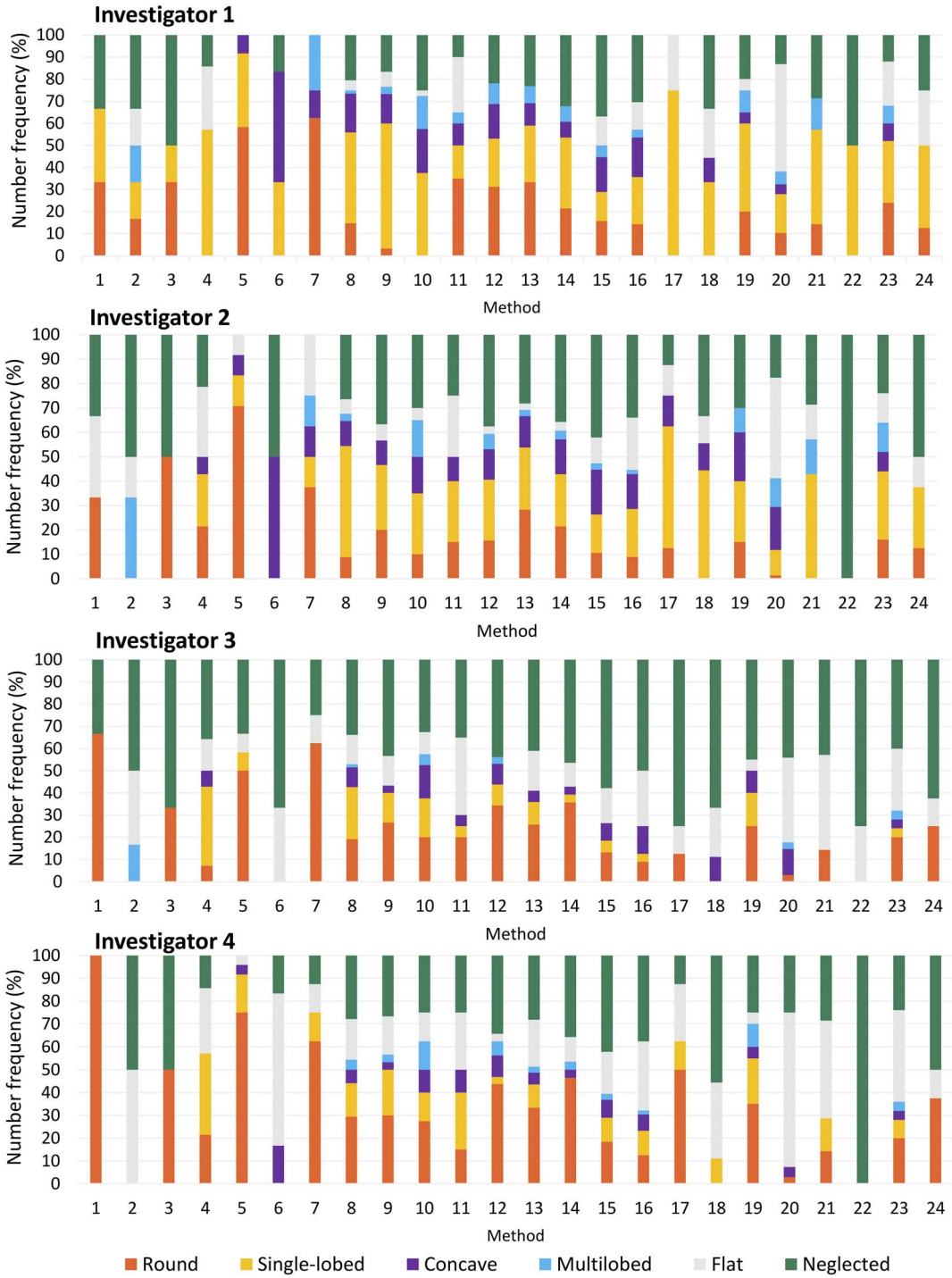

Fig. 4 Shape classification of extracellular vesicles using the in-house developed EVIAN program in Python: distribution of particles based on shape across different methods as classified by four investigators. Legend for methods: without fixation + air-dried (1 – $NiCl_2$, 2 – PLL, 3 – APTES-v, 4 – APTES-l); fixed + air-dried (5 – $NiCl_2$, 6 – PLL, 7 – APTES-v, 8 – APTES-l); fixed + EtOH + CPD (9 – $NiCl_2$, 10 – PLL, 11 – APTES-v, 12 – APTES-l); fixed + DMP + CPD (13 – $NiCl_2$, 14 – PLL, 15 – APTES-v, 16 – APTES-l); fixed + EtOH + HMDS (17 – $NiCl_2$, 18 – PLL, 19 – APTES-v, 20 – APTES-l); fixed + DMP + HMDS (21 – $NiCl_2$, 22 – PLL, 23 – APTES-v, 24 – APTES-l).

methods (Fig. 3b). Such flattening might be a consequence of too strong adhesion of EVs to the amino-functionalised mica, as has been observed before for high concentrations of APTES.[57] HMDS might contribute to this effect too, since such flattening was the most obvious when HMDS was used. On the other hand, the low aspect ratios for method 8 seem to have arisen more from single-lobed structures, possibly due to deformations during simple air drying. Otherwise, round and/or single-lobed shapes dominated in most of the samples, while flat, concave and especially multilobed structures were in minority. Method 5

($NiCl_2$ + fixative and air-drying) yielded the largest fraction of round particles and a very low fraction of concave, flat or neglected particles.

We can see that different preparation methods can give many different size and shape distributions for the same sample of EVs without even introducing any variations in the isolation method. Therefore, a standardised and reliable sample preparation is key for successful morphological analysis, consistency and reproducibility. Moreover, variability in shape classification is evident for four independent researchers who analysed the same images. To resolve this, we need to better define the shape classes, and use better resolution and larger areas that would capture larger, statistically more representative samples.

Shape definition is challenging with complex three-dimensional and ambiguous particles. Certain structures will often be at the edge, overlapping the different shape class characteristics. Kapoor *et al.* applied similar logic as in this study and successfully categorized different shapes of EVs from cryo-TEM images to single spherical, tubular and double, choosing eccentricity as a quantitative metric for defining shape but also the diameter, and major and minor axes.[58]

Challenges also remain in achieving reproducibility and accuracy in EV research. Higher resolution imaging can enhance the accuracy of morphological assessments, aiding in the distinction of subtle differences between EV subpopulations. However, the trade-off between resolution and acquisition time should be carefully considered.[59] And not only the imaging efficiency, but shape categorisation efficiency should also be considered. The use of a computer program EVIAN for selection, displaying and manual classification notably shortened the time of morphological analysis but with higher resolution and an increased number of particles, this would still become overly time consuming. It could be greatly improved if we switched from manual to automated shape classification. That is why we created a training set for ML from 231 grains, for which all 4 investigators selected exactly the same shape designation. It contained 56 round, 16 single-lobed, 15 concave, 3 multilobed, 26 flat and 115 neglected particles.

3.3. Machine learning in EV classification by morphology

The machine learning outcome is illustrated by a confusion matrix, which evaluated the model's ability to correctly recognise each EV shape (Fig. 5a). The model excelled at identifying round EVs and artefacts (the "neglect" class), likely due to their distinct morphological characteristics and the most abundant presence in the dataset. In contrast, the multilobed class, which had only three instances in the dataset, exhibited the highest misclassification rate, often being confused with other classes. This can be attributed to both the small sample size and the morphological similarities between the multilobed and other classes. Hence, the model's performance is consistent with the class distribution in the dataset, which is typical in cases of class imbalance in the training dataset, despite the efforts to mitigate this through data augmentation and SMOTE.[37] Interestingly, the concave and flat particles, though not as well-represented as round and neglected, were classified with relatively high accuracy. This suggests that these morphologies possess distinguishing features that the model was able to learn effectively, even with fewer training examples. In total, 50 predictive models were trained and evaluated independently. The best-performing model, identified through grid search with a batch size of 32, 150 training epochs, and the Adam optimizer, demonstrated an average test accuracy of 85.28% and a weighted F_1 score of 85.44%, with a standard deviation of 5.07% and 4.75%, respectively. This consistency in performance highlights the robustness of the model across different data splits. The ability of the model to neglect the artefacts very well is particularly promising for retrieving correct EV size distributions from AFM images, even more closely than when manual analysis approximated those measured by DLS and previous measurements with other methods on similar samples of EVs from CSF.[22,40]

The best performing model was then used to analyse the same 567 grains from the 24 AFM images as the four investigators. Fig. 5b shows thus obtained EV shape distributions for the 24 methods. It is in very good agreement with the manually generated distributions. Among images with at least 15 EVs/100 μm, distributions of samples 8, 9, 11 and 23 agree best with the results of Investigator 1; samples 10 and 12 with Investigator 2; 14–16 with Investigator 3; 5, 13 and 20 with Investigator 4. The automated analysis by the CNN model[36] also detected the largest fraction of flat structures in the case of APTES-l + fixative + ethanol gradient + HMDS (method 20) and the highest frequency of round particles in the case of $NiCl_2$ functionalisation with air-drying after fixation (method 5). In the majority of samples, the histograms of max. *D* were peaked between 100 and 150 nm, which is very much in agreement with DLS, especially if also considering the increased apparent size in DLS due to hydration (Fig. S4). Most max. *H* distributions exhibit a maximum between 20 and 40 nm (Fig. S5). The majority of particles for methods 8, 10, 13–16, 20 and 23 are below 50 nm high, while there is a non-negligible fraction of particles with larger heights for the other 4 protocols (5, 9, 11 and 12, Fig. S5). The most common aspect ratio was 0.2–0.3 for methods 5, 8, 16, 20 and 23, for which these distributions were narrow, as in the case of protocol 11, which yielded even lower (0.1–0.2) max. *H*/max. *D* ratios, confirming the flattening effect (Fig. S6). The distributions for methods 13–15 were similar but slightly wider, while they appeared almost normal for methods 10 and 12, with modes at 0.3–0.4 and the range extending from 0.1 to 0.6 (Fig. S6). Method 9 stands out exhibiting two modes, with the second one above 0.4, and the range extended up to 0.7.

Generally, taking all morphometrics (dimension ranges and distributions, aspect ratio ranges and distributions and shape distributions) together, we can conclude that drying from HMDS (methods 17–24) is not a good option for preparation of EVs for visualisation by AFM, as it either causes detachment of EVs from the functionalised surface (methods 17–19, 21, 22 and 24), flattening (method 20) or deformations leading to ambiguous shapes (method 23). By contrast, dehydration of fixed EVs in ethanol gradient followed by CPD (methods 9, 10 and 12) seems the most optimal preparation protocol, as it yielded EVs with the highest aspect ratios, a solid number of captured EVs, a relatively

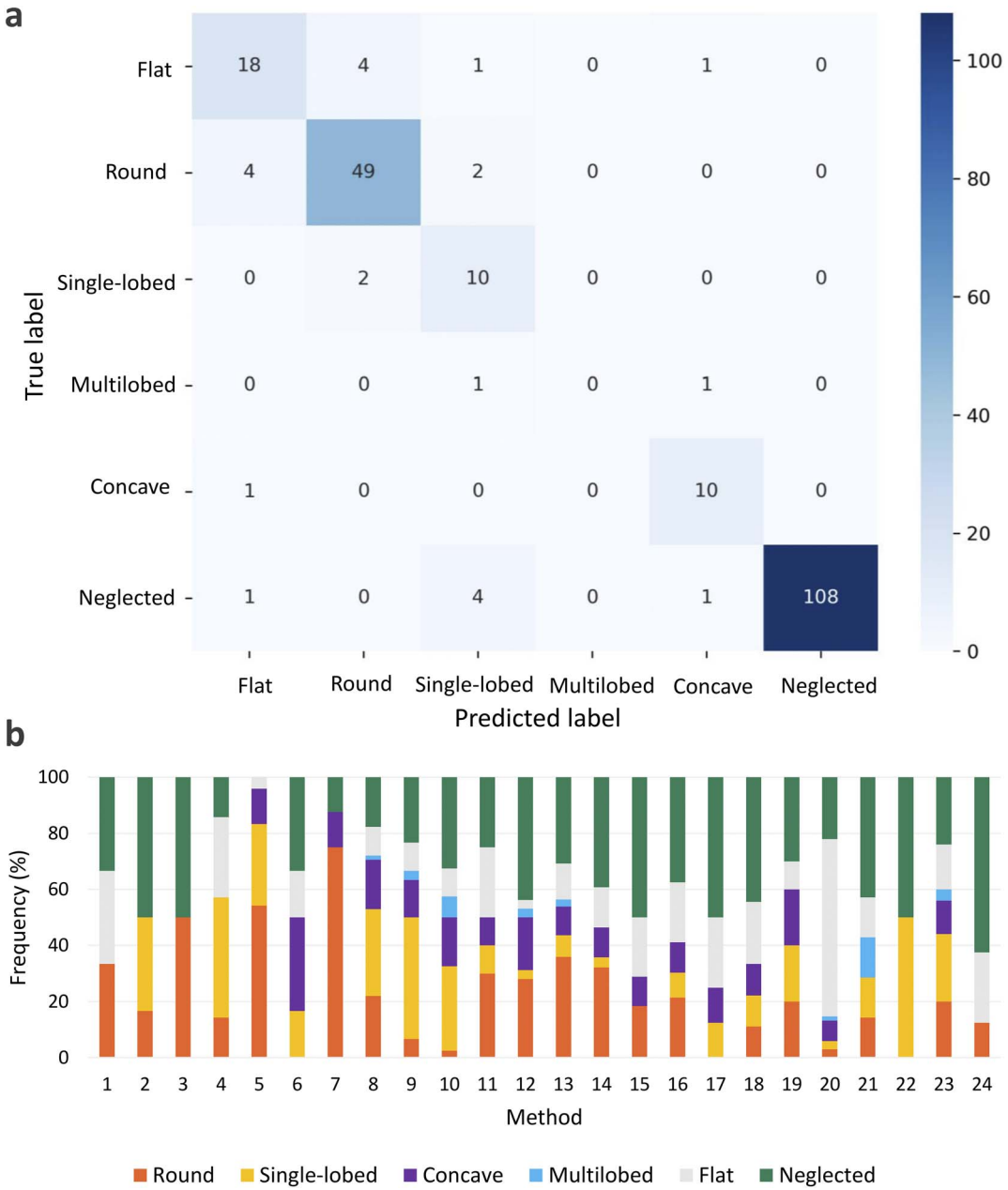

Fig. 5 The confusion matrix in panel (a) displays the classification performance of the machine learning model, with values averaged across 10 iterations of 5-fold cross-validation, showing true and predicted particle shapes. Panel (b) presents the distribution of particles based on shape, as classified by the machine learning model, across 24 different methods. Legend for methods: without fixation + air-dried (1 – $NiCl_2$, 2 – PLL, 3 – APTES-v, 4 – APTES-l); fixed + air-dried (5 – $NiCl_2$, 6 – PLL, 7 – APTES-v, 8 – APTES-l); fixed + EtOH + CPD (9 – $NiCl_2$, 10 – PLL, 11 – APTES-v, 12 – APTES-l); fixed + DMP + CPD (13 – $NiCl_2$, 14 – PLL, 15 – APTES-v, 16 – APTES-l); fixed + EtOH + HMDS (17 – $NiCl_2$, 18 – PLL, 19 – APTES-v, 20 – APTES-l); fixed + DMP + HMDS (21 – $NiCl_2$, 22 – PLL, 23 – APTES-v, 24 – APTES-l).

low fraction of neglected particles, a low fraction of concave shapes and either round or single-lobed as the most frequent shape. Moreover, while APTES functionalisation needs some further optimisation in terms of the functionaliser amount and technique of functionalisation, as they sometimes resulted in poor EV capture and flattening, $NiCl_2$ coating gave the most intriguing and somewhat puzzling results, with air drying rendering rounder structures, ethanol gradient with CPD predominantly leading to single-lobed structures with expected EV size and the highest aspect ratios, and chemical dehydration with DMP, followed by CPD, resulting in particle shape and size distributions very similar to those after the other functionalisations.

To resolve whether round nanoparticles get lost during additional dehydration and drying steps or they emerge as a result of air drying, and to further enhance the objectivity of the preparation protocol comparison, we analysed two times larger area for methods 5 ($NiCl_2$, fixative and air-drying), 9

($NiCl_2$, fixative, ethanol gradient and CPD) and 13 ($NiCl_2$, fixative, DMP and CPD) and added liquid AFM (no dehydration and drying) for EVs on $NiCl_2$-coated mica as a reference of their "true" (near-native) dimensions and shapes (Fig. 6). We used the CNN model for artefact elimination and shape classification. All three dried samples exhibited slightly smaller most frequent max. *D* than the non-dried sample (100–150 nm mode, while it was 150–200 nm for the non-dried sample, Fig. 6(i)), but the differences in the size distributions were not statistically significantly different. By contrast, all four methods revealed the most abundant max. *H* between 30 and 40 nm. However, method 5 was statistically significantly different from the liquid AFM method in the height distribution ($p = 0.013$ by the two-tailed Mann–Whitney *U* test, Fig. 6(ii)). The deviation of this method from liquid AFM was even more evident in the aspect ratio distributions as there was less than 0.5% probability ($p = 0.0028$) that method 5 and liquid AFM data came from the same sample. Although all four aspect ratio distributions were peaked at 0.2–0.3, EVs with aspect ratios above 0.5 existed only in the non-dried sample and dried sample based on method 9, which even exhibited another maximum at 0.4–0.5 (Fig. 6(iii)). Moreover, the shape distribution of method 9 also most closely resembled the one of the non-dried sample (it is the only one of the three dried samples for which round is not the most common shape), although all three AFM air methods overexpressed round shapes with regards to near-native liquid AFM morphology (Fig. 6(iv)). On the other hand, the max. *H* distribution of method 13 agreed best with the liquid AFM data (Fig. 6(ii)). Hence, we can conclude that crytical point drying is crucial for preserving the near-native morphology of EVs in examination by AFM in air and both chemical or ethanol gradient dehydrations function well, but the ethanol gradient better preserves particles with a higher aspect ratio. There is room for optimisation in $NiCl_2$ functionalisation, which seems to cause some round artefacts or rounding of EVs. It is not yet known whether the various observed morphologies distinctively differ in certain biochemical properties. Furthermore, EVs can undergo different topological changes affected by the presence

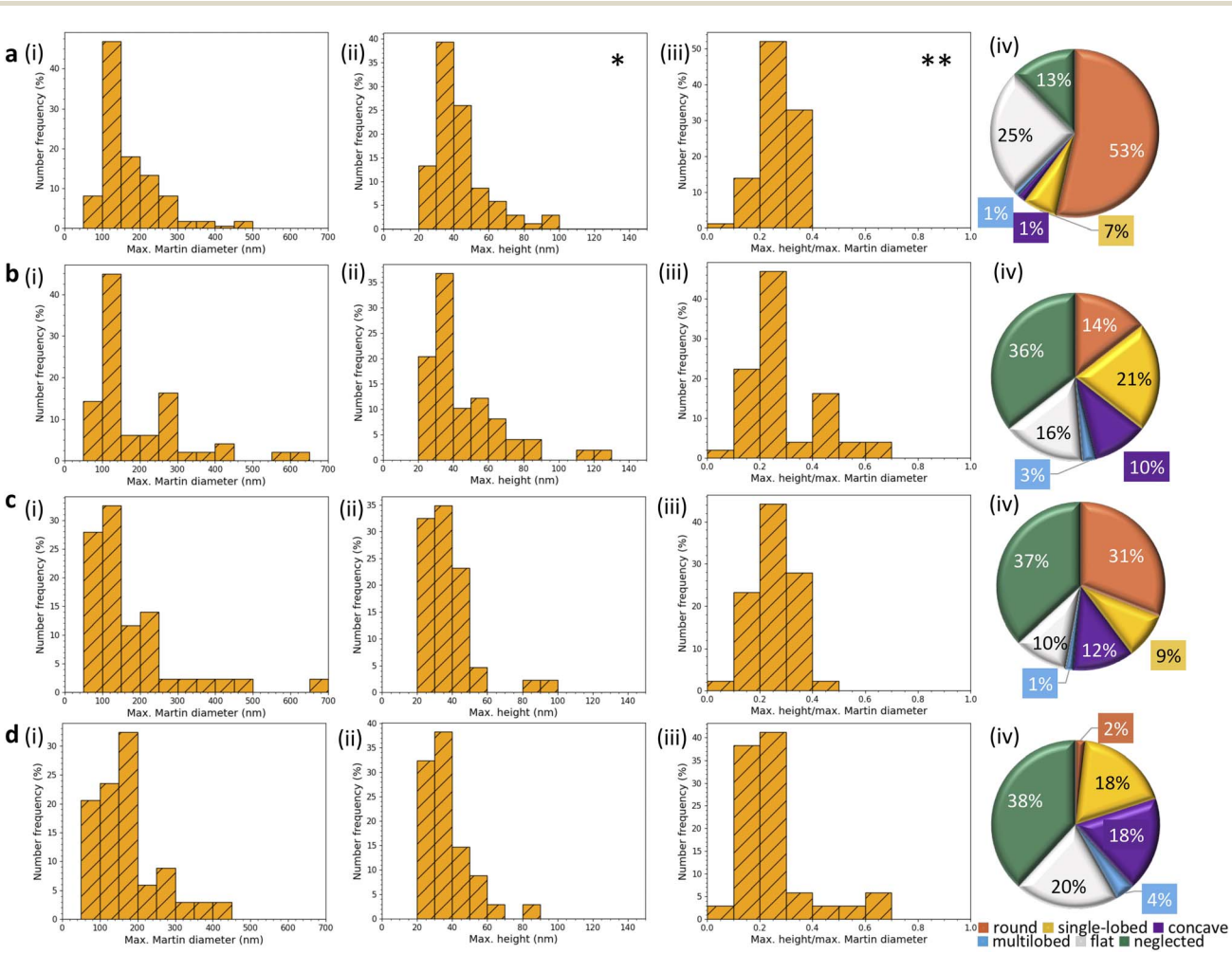

Fig. 6 Comparison of morphometric characteristics (maximum Martin diameter distribution (i), maximum height distribution (ii), aspect ratio (maximum height/maximum Martin diameter) distribution (iii) and shape distribution (iv)) of EVs on $NiCl_2$-coated mica prepared by 4 different methods (5 (a), 9 (b), 13 (c) and liquid AFM (d)). One asterisk (*) denotes a statistically significant difference in comparison with the liquid AFM image ($p < 0.05$) and two asterisks (**) denote a statistically significant difference in comparison with the liquid AFM image ($p < 0.005$) after Mann–Whitney *U* analysis.

of different molecules.[3] Future addition of immune-based detections after reliable morphology determination and quantification should resolve this. Nevertheless, using immunolabeling with functionalised Au nanoparticles based on the proteins identified by western blotting, Harrington *et al.*[60] discovered that only spherical nanostructures contained the exosome-associated protein. This indicated that the nanospheres could be involved in neurotransmission and signal transduction/regulatory activities within CSF, whereas nanosized blobs and strands have an important connective/adhesive role in neurite development. Only the spheres with 80–100 nm diameters were immunolabelled with antibodies against acetylcholine, which indicates that only the bigger EVs are involved in neurotransmission. Sharma *et al.*[61] detected a single molecule of transmembrane protein CD63 on the surface of EVs from saliva with an antibody-coated tip and antibody-labelled gold beads enabling the detection of specific membrane markers for specific diseases. Furthermore, comparison of topographic images of UC-isolated exosomes from the saliva of healthy individuals and the saliva of oral cancer patients revealed that normal exosomes exhibited a circular, homogeneous, bulging structure and diameter of 40–80 nm, while cancer-originating exosomes were bigger, with a broader distribution of 20–400 nm and manifested irregular morphologies, aggregation and clustering. Also, cancer exosomes indicated a possible increased surface CD63 density.[62]

All in all, we can say that we successfully provided an automated platform for classifying and quantifying EVs from AFM images and the model achieved high accuracy and F_1 scores overall. Nevertheless, we can see several possibilities for improvement.

First, the limited number of instances in certain classes, such as multilobed, suggests that more labelled data are needed to improve shape categorisation accuracy. In future work, acquiring additional EV samples, particularly for underrepresented classes, will be critical for improving the performance of this model.

Moreover, while data augmentation and SMOTE were effective in balancing the class distribution and enhancing model stability more advanced augmentation techniques – such as generative adversarial networks – could be explored to create more realistic synthetic samples. This would further reduce the impact of class imbalance and improve the model's ability to generalize rare EV morphologies.

Finally, the current model architecture could be further optimized by expanding investigations to a broader range of EV morphologies, particularly underrepresented classes, analysing AFM images in a higher resolution and in a liquid/native environment, and exploring alternative deep learning approaches, such as transfer learning or more complex network architectures, to enhance feature extraction and improve classification performance.

4. Conclusion

This investigation has demonstrated that the sample preparation protocol can influence the morphology of EVs. Ethanol gradient dehydration followed by critical point drying best preserved the EV morphology with the highest aspect ratios when applied on $NiCl_2$-coated mica, for which all morphometric data agreed very well with the near-native EV morphology observed in liquid AFM images.

The structure of EVs cannot be unambiguously and easily resolved by manual morphological analysis, even with the assistance of a computer program to display individual particles and export their morphological classifications. Such a task soon becomes either too demanding and time consuming for reliable data collection or results in a dataset too small to draw trustworthy conclusions. Here, we obtained a sufficiently large dataset to train and develop a CNN to distinguish between the various EV morphologies that we observed and defined. After training, the model achieved a high level of accuracy, with an F_1 score of 85 $\pm$ 5%. It is particularly important that the CNN demonstrated a strong ability to disregard artefacts captured during non-topological automatic grain detection and analysis in Gwyddion. This enables more accurate determination of sizes and size distributions of EVs based on AFM images. The successful integration of ML in this context signifies a key advancement in the analysis of EV morphology, mitigating the subjectivity and time inefficiency of manual categorisations. CNNs will be able to process a much larger amount of data in a notably shorter time. Consequently, reproducibility and accuracy will improve, which will greatly enhance the implementation of the AFM images in liquid biopsies, facilitating non-invasive monitoring. In this manuscript, we present a tool for future research that will (i) facilitate and greatly improve the standardisation of sample isolation and preparation protocols to better preserve the native morphology of EVs and (ii) incorporate additional features, such as biomechanics and immunobased profiling. By correlating morphology, topology and other physical properties with specific biomolecular signatures, the genesis and biological role of each EV class could be elucidated. Inability to monitor the brain's cellular and metabolic state at micro- and nano-levels continuously is a major limitation in TBI treatment and discovery of brain-related diseases. Here, the presented results and inventions are an important step towards precise and proactive diagnostics and treatment in the future.

Author contributions

M. M., M. K. and I. Š. designed the experiments, integrated the studies and wrote the manuscript. M. P., V. T., H. K., L. S. M. and J. T. conducted investigations and prepared the results. I. Š. and L. I. developed the ML model. M. K. and D. F. wrote the EVIAN program. V. T., M. T., M. K. and M. M. conducted shape analysis. M. K. and M. M. reviewed & edited the manuscript. All authors checked the manuscript.

Conflicts of interest

There are no conflicts to declare.

Data availability

Data for this article, including AFM images, dynamic light scattering and zeta potential data, machine learning, automated analysis of EV morphology, statistical analysis, Gwyddion data, and western blot/immunoblot images are available at Dabar at **https://urn.nsk.hr/urn:nbn:hr:184:359174**.[63]

The code for the EVIAN program for manual classification of vesicles (or other notable features) imaged by AFM can be found at **https://github.com/David-Fabijan/EVIAN** with DOI **https://doi.org/10.5281/zenodo.17245737**.[35] The version of the code employed for this study is 0.9.

The study was conducted according to the guidelines of the Declaration of Helsinki, and approved by the Ethics Committee of General Hospital Pula, Pula, Croatia (number: 4943/10-1, 17 July 2019). Informed consent was obtained from a family member for all TBI patients and cannot be made available due to ethical confidentiality requirements.

Additional data are available from the corresponding author upon reasonable request.

Data generated and analysed during this study are included in this published article and its supplementary information (SI) files. Supplementary information is available. See DOI: **https://doi.org/10.1039/d5na00665a**.

Acknowledgements

This work has been supported in part by the University of Rijeka grants under the project numbers: uniri-biomed-18-279, uniri-iskusni-biomed-23-169, UNIRI-INOVA-1-22-4, and UNIRI-INOVA-4-24-6 and The Foundation of the Croatian Academy of Sciences and Arts (grants to M. M.). We would like to thank Siniša Zrna and Maša Biberić for collecting the patient samples and providing the patient data.

References

1 D. K. Jeppesen, Q. Zhang, J. L. Franklin and R. J. Coffey, *Trends Cell Biol.*, 2023, **33**, 667–681.
2 H. M. Ramos-Zaldívar, I. Polakovicova, E. Salas-Huenuleo, A. H. Corvalán, M. J. Kogan, C. P. Yefi and M. E. Andia, *Fluids Barriers CNS*, 2022, **19**, 60.
3 M. Bottacchiari, M. Gallo, M. Bussoletti and C. M. Casciola, *PNAS Nexus*, 2024, **3**, pgae300.
4 M. Xiong, Z. Chen, J. Tian, Y. Peng, D. Song, L. Zhang and Y. Jin, *Cell Commun. Signaling*, 2024, **22**, 156.
5 A. Manolopoulos, P. J. Yao and D. Kapogiannis, *Nat. Rev. Neurol.*, 2025, **21**, 265–282.
6 D. J. Beetler, D. N. Di Florio, K. A. Bruno, T. Ikezu, K. L. March, L. T. Cooper, J. Wolfram and D. Fairweather, *Mol. Aspects Med.*, 2023, **91**, 101155.
7 M. A. Kumar, S. K. Baba, H. Q. Sadida, S. A. Marzooqi, J. Jerobin, F. H. Altemani, N. Algehainy, M. A. Alanazi, A.-B. Abou-Samra, R. Kumar, A. S. Al-Shabeeb Akil, M. A. Macha, R. Mir and A. A. Bhat, *Signal Transduction Targeted Ther.*, 2024, **9**, 1–41.
8 E. Eren, J.-M. Leoutsakos, J. Troncoso, C. G. Lyketsos, E. S. Oh and D. Kapogiannis, *Cells*, 2022, **11**, 436.
9 Y. You, S. Muraoka, M. P. Jedrychowski, J. Hu, A. K. McQuade, T. Young-Pearse, R. Aslebagh, S. A. Shaffer, S. P. Gygi, M. Blurton-Jones, W. W. Poon and T. Ikezu, *J. Extracell. Vesicles*, 2022, **11**, e12183.
10 S. Herman, R. Djaldetti, B. Mollenhauer and D. Offen, *Brain*, 2023, **146**, 209–224.
11 S. Chen, Q. Bao, W. Xu and X. Zhai, *J. Nanobiotechnol.*, 2025, **23**, 263.
12 C. Théry, K. W. Witwer, E. Aikawa, M. J. Alcaraz, J. D. Anderson, R. Andriantsitohaina, A. Antoniou, T. Arab, F. Archer, G. K. Atkin-Smith, D. C. Ayre, J.-M. Bach, D. Bachurski, H. Baharvand, L. Balaj, S. Baldacchino, N. N. Bauer, A. A. Baxter, M. Bebawy, C. Beckham, A. B. Zavec, A. Benmoussa, A. C. Berardi, P. Bergese, E. Bielska, C. Blenkiron, S. Bobis-Wozowicz, E. Boilard, W. Boireau, A. Bongiovanni, F. E. Borràs, S. Bosch, C. M. Boulanger, X. Breakefield, A. M. Breglio, M. Á. Brennan, D. R. Brigstock, A. Brisson, M. L. Broekman, J. F. Bromberg, P. Bryl-Górecka, S. Buch, A. H. Buck, D. Burger, S. Busatto, D. Buschmann, B. Bussolati, E. I. Buzás, J. B. Byrd, G. Camussi, D. R. Carter, S. Caruso, L. W. Chamley, Y.-T. Chang, C. Chen, S. Chen, L. Cheng, A. R. Chin, A. Clayton, S. P. Clerici, A. Cocks, E. Cocucci, R. J. Coffey, A. Cordeiro-da-Silva, Y. Couch, F. A. Coumans, B. Coyle, R. Crescitelli, M. F. Criado, C. D'Souza-Schorey, S. Das, A. D. Chaudhuri, P. de Candia, E. F. D. S. Junior, O. D. Wever, H. A. del Portillo, T. Demaret, S. Deville, A. Devitt, B. Dhondt, D. D. Vizio, L. C. Dieterich, V. Dolo, A. P. D. Rubio, M. Dominici, M. R. Dourado, T. A. Driedonks, F. V. Duarte, H. M. Duncan, R. M. Eichenberger, K. Ekström, S. E. Andaloussi, C. Elie-Caille, U. Erdbrügger, J. M. Falcón-Pérez, F. Fatima, J. E. Fish, M. Flores-Bellver, A. Försönits, A. Frelet-Barrand, F. Fricke, G. Fuhrmann, S. Gabrielsson, A. Gámez-Valero, C. Gardiner, K. Gärtner, R. Gaudin, Y. S. Gho, B. Giebel, C. Gilbert, M. Gimona, I. Giusti, D. C. Goberdhan, A. Görgens, S. M. Gorski, D. W. Greening, J. C. Gross, A. Gualerzi, G. N. Gupta, D. Gustafson, A. Handberg, R. A. Haraszti, P. Harrison, H. Hegyesi, A. Hendrix, A. F. Hill, F. H. Hochberg, K. F. Hoffmann, B. Holder, H. Holthofer, B. Hosseinkhani, G. Hu, Y. Huang, V. Huber, S. Hunt, A. G.-E. Ibrahim, T. Ikezu, J. M. Inal, M. Isin, A. Ivanova, H. K. Jackson, S. Jacobsen, S. M. Jay, M. Jayachandran, G. Jenster, L. Jiang, S. M. Johnson, J. C. Jones, A. Jong, T. Jovanovic-Talisman, S. Jung, R. Kalluri, S. Kano, S. Kaur, Y. Kawamura, E. T. Keller, D. Khamari, E. Khomyakova, A. Khvorova, P. Kierulf, K. P. Kim, T. Kislinger, M. Klingeborn, D. J. K. Klinke II, M. Kornek, M. M. Kosanović, Á. F. Kovács, E.-M. Krämer-Albers, S. Krasemann, M. Krause, I. V. Kurochkin, G. D. Kusuma, S. Kuypers, S. Laitinen, S. M. Langevin, L. R. Languino, J. Lannigan, C. Lässer, L. C. Laurent, G. Lavieu, E. Lázaro-Ibáñez, S. L. Lay, M.-S. Lee, Y. X. F. Lee, D. S. Lemos, M. Lenassi, A. Leszczynska, I. T. Li, K. Liao, S. F. Libregts,

E. Ligeti, R. Lim, S. K. Lim, A. Linē, K. Linnemannstöns, A. Llorente, C. A. Lombard, M. J. Lorenowicz, Á. M. Lörincz, J. Lötvall, J. Lovett, M. C. Lowry, X. Loyer, Q. Lu, B. Lukomska, T. R. Lunavat, S. L. Maas, H. Malhi, A. Marcilla, J. Mariani, J. Mariscal, E. S. Martens-Uzunova, L. Martin-Jaular, M. C. Martinez, V. R. Martins, M. Mathieu, S. Mathivanan, M. Maugeri, L. K. McGinnis, M. J. McVey, D. G. Meckes Jr, K. L. Meehan, I. Mertens, V. R. Minciacchi, A. Möller, M. M. Jørgensen, A. Morales-Kastresana, J. Morhayim, F. Mullier, M. Muraca, L. Musante, V. Mussack, D. C. Muth, K. H. Myburgh, T. Najrana, M. Nawaz, I. Nazarenko, P. Nejsum, C. Neri, T. Neri, R. Nieuwland, L. Nimrichter, J. P. Nolan, E. N. N.-'t. Hoen, N. N. Hooten, L. O'Driscoll, T. O'Grady, A. O'Loghlen, T. Ochiya, M. Olivier, A. Ortiz, L. A. Ortiz, X. Osteikoetxea, O. Østergaard, M. Ostrowski, J. Park, D. M. Pegtel, H. Peinado, F. Perut, M. W. Pfaffl, D. G. Phinney, B. C. Pieters, R. C. Pink, D. S. Pisetsky, E. P. von Strandmann, I. Polakovicova, I. K. Poon, B. H. Powell, I. Prada, L. Pulliam, P. Quesenberry, A. Radeghieri, R. L. Raffai, S. Raimondo, J. Rak, M. I. Ramirez, G. Raposo, M. S. Rayyan, N. Regev-Rudzki, F. L. Ricklefs, P. D. Robbins, D. D. Roberts, S. C. Rodrigues, E. Rohde, S. Rome, K. M. Rouschop, A. Rughetti, A. E. Russell, P. Saá, S. Sahoo, E. Salas-Huenuleo, C. Sánchez, J. A. Saugstad, M. J. Saul, R. M. Schiffelers, R. Schneider, T. H. Schøyen, A. Scott, E. Shahaj, S. Sharma, O. Shatnyeva, F. Shekari, G. V. Shelke, A. K. Shetty, K. Shiba, P. R.-M. Siljander, A. M. Silva, A. Skowronek, O. L. Snyder II, R. P. Soares, B. W. Sódar, C. Soekmadji, J. Sotillo, P. D. Stahl, W. Stoorvogel, S. L. Stott, E. F. Strasser, S. Swift, H. Tahara, M. Tewari, K. Timms, S. Tiwari, R. Tixeira, M. Tkach, W. S. Toh, R. Tomasini, A. C. Torrecilhas, J. P. Tosar, V. Toxavidis, L. Urbanelli, P. Vader, B. W. van Balkom, S. G. van der Grein, J. V. Deun, M. J. van Herwijnen, K. V. Keuren-Jensen, G. van Niel, M. E. van Royen, A. J. van Wijnen, M. H. Vasconcelos, I. J. Vechetti Jr, T. D. Veit, L. J. Vella, É. Velot, F. J. Verweij, B. Vestad, J. L. Viñas, T. Visnovitz, K. V. Vukman, J. Wahlgren, D. C. Watson, M. H. Wauben, A. Weaver, J. P. Webber, V. Weber, A. M. Wehman, D. J. Weiss, J. A. Welsh, S. Wendt, A. M. Wheelock, Z. Wiener, L. Witte, J. Wolfram, A. Xagorari, P. Xander, J. Xu, X. Yan, M. Yáñez-Mó, H. Yin, Y. Yuana, V. Zappulli, J. Zarubova, V. Žėkas, J. Zhang, Z. Zhao, L. Zheng, A. R. Zheutlin, A. M. Zickler, P. Zimmermann, A. M. Zivkovic, D. Zocco and E. K. Zuba-Surma, *J. Extracell. Vesicles*, 2018, **7**, 1535750.

13 J. A. Welsh, D. C. I. Goberdhan, L. O'Driscoll, E. I. Buzas, C. Blenkiron, B. Bussolati, H. Cai, D. Di Vizio, T. A. P. Driedonks, U. Erdbrügger, J. M. Falcon-Perez, Q.-L. Fu, A. F. Hill, M. Lenassi, S. K. Lim, M. G. Mahoney, S. Mohanty, A. Möller, R. Nieuwland, T. Ochiya, S. Sahoo, A. C. Torrecilhas, L. Zheng, A. Zijlstra, S. Abuelreich, R. Bagabas, P. Bergese, E. M. Bridges, M. Brucale, D. Burger, R. P. Carney, E. Cocucci, R. Crescitelli, E. Hanser, A. L. Harris, N. J. Haughey, A. Hendrix, A. R. Ivanov, T. Jovanovic-Talisman, N. A. Kruh-Garcia, V. Ku'ulei-Lyn Faustino, D. Kyburz, C. Lässer, K. M. Lennon, J. Lötvall, A. L. Maddox, E. S. Martens-Uzunova, R. R. Mizenko, L. A. Newman, A. Ridolfi, E. Rohde, T. Rojalin, A. Rowland, A. Saftics, U. S. Sandau, J. A. Saugstad, F. Shekari, S. Swift, D. Ter-Ovanesyan, J. P. Tosar, Z. Useckaite, F. Valle, Z. Varga, E. van der Pol, M. J. C. van Herwijnen, M. H. M. Wauben, A. M. Wehman, S. Williams, A. Zendrini, A. J. Zimmerman, MISEV Consortium, C. Théry and K. W. Witwer, *J. Extracell. Vesicles*, 2024, **13**, e12404.

14 S. A. Gazze, S. J. Thomas, J. Garcia-Parra, D. W. James, P. Rees, V. Marsh-Durban, R. Corteling, D. Gonzalez, R. S. Conlan and L. W. Francis, *Nanoscale*, 2021, **13**, 6129–6141.

15 M. LeClaire, J. Gimzewski and S. Sharma, *Nano Sel.*, 2021, **2**, 1–15.

16 I. Sokolov, *Phys. Chem. Chem. Phys.*, 2024, **26**, 11263–11270.

17 D. Vorselen, S. M. van Dommelen, R. Sorkin, M. C. Piontek, J. Schiller, S. T. Döpp, S. A. A. Kooijmans, B. A. van Oirschot, B. A. Versluijs, M. B. Bierings, R. van Wijk, R. M. Schiffelers, G. J. L. Wuite and W. H. Roos, *Nat. Commun.*, 2018, **9**, 4960.

18 M. Malenica, M. Vukomanović, M. Kurtjak, V. Masciotti, S. Dal Zilio, S. Greco, M. Lazzarino, V. Krušić, M. Perčić, I. Jelovica Badovinac, K. Wechtersbach, I. Vidović, V. Baričević, S. Valić, P. Lučin, N. Kojc and K. Grabušić, *Biomedicines*, 2021, **9**, 603.

19 M. Skliar and V. S. Chernyshev, *J. Visualized Exp.*, 2019, **151**, e59254.

20 D. Vorselen, F. C. MacKintosh, W. H. Roos and G. J. L. Wuite, *ACS Nano*, 2017, **11**, 2628–2636.

21 A. Emelyanov, T. Shtam, R. Kamyshinsky, L. Garaeva, N. Verlov, I. Miliukhina, A. Kudrevatykh, G. Gavrilov, Y. Zabrodskaya, S. Pchelina and A. Konevega, *PLoS One*, 2020, **15**, e0227949.

22 M. Kurtjak, S. Kereïche, D. Klepac, H. Križan, M. Perčić, V. Krušić Alić, T. Lavrin, M. Lenassi, K. Wechtersbach, N. Kojc, M. Vukomanović, S. Zrna, M. Biberić, R. Domitrović, K. Grabušić and M. Malenica, *Biomedicines*, 2022, **10**, 1251.

23 C. del Real Mata, O. Jeanne, M. Jalali, Y. Lu and S. Mahshid, *Adv. Healthcare Mater.*, 2023, **12**, 2202123.

24 A. Uthamacumaran, M. Abdouh, K. Sengupta, Z. Gao, S. Forte, T. Tsering, J. V. Burnier and G. Arena, *Neural Computing and Applications*, 2023, **35**, 8407–8422.

25 M. N. Jensen, E. M. Guerreiro, A. Enciso-Martinez, S. G. Kruglik, C. Otto, O. Snir, B. Ricaud and O. G. Hellesø, *Sci. Rep.*, 2024, **14**, 6791.

26 X. Pu, C. Zhang, G. Ding, H. Gu, Y. Lv, T. Shen, T. Pang, L. Cao and S. Jia, *Transl. Oncol.*, 2024, **40**, 101847.

27 X.-W. Zhang, G.-X. Qi, M.-X. Liu, Y.-F. Yang, J.-H. Wang, Y.-L. Yu and S. Chen, *ACS Sens.*, 2024, **9**, 1555–1564.

28 E. Cansever Mutlu, M. Kaya, I. Küçük, B. Ben-Nissan and A. Stamboulis, *Materials*, 2022, **15**, 7967.

29 K. Ito, Y. Ogawa, K. Yokota, S. Matsumura, T. Minamisawa, K. Suga, K. Shiba, Y. Kimura, A. Hirano-Iwata,

Y. Takamura and T. Ogino, *J. Phys. Chem. B*, 2018, **122**, 6224–6235.
30 T. Uchihashi, H. Watanabe and N. Kodera, in *Nanoscale Imaging*, ed. Y. L. Lyubchenko, Springer New York, New York, NY, 2018, vol. 1814, pp. 159–179.
31 A. M. Bronder, A. Bieker, S. Elter, M. Etzkorn, D. Häussinger and F. Oesterhelt, *Biophys. J.*, 2016, **111**, 1925–1934.
32 Y. Qin, W. Jiang, A. Li, M. Gao, H. Liu, Y. Gao, X. Tian and G. Gong, *Biomolecules*, 2021, **11**, 711.
33 D. B. Nguyen, T. B. Thuy Ly, M. C. Wesseling, M. Hittinger, A. Torge, A. Devitt, Y. Perrie and I. Bernhardt, *Cell. Physiol. Biochem.*, 2016, **38**, 1085–1099.
34 K. Conway and J. A. Kiernan, *Biotech. Histochem.*, 1999, **74**, 20–26.
35 M. Kurtjak and D. Fabijan, *GitHub, EVIAN program in Python*, 2024, DOI: **10.5281/zenodo.17245737**.
36 I. Goodfellow, Y. Bengio and A. Courville, *Deep Learning*, MIT Press, 2016.
37 N. V. Chawla, K. W. Bowyer, L. O. Hall and W. P. Kegelmeyer, *J. Artif. Intell. Res.*, 2002, **16**, 321–357.
38 U. S. Sandau, S. M. Magaña, J. Costa, J. P. Nolan, T. Ikezu, L. J. Vella, H. K. Jackson, L. R. Moreira, P. L. Palacio, A. F. Hill, J. F. Quinn, K. R. Van Keuren-Jensen, T. J. McFarland, J. Palade, E. A. Sribnick, H. Su, K. Vekrellis, B. Coyle, Y. Yang, J. M. Falcón-Perez, R. Nieuwland, J. A. Saugstad and International Society for Extracellular Vesicles Cerebrospinal Fluid Task Force, *J. Extracell. Vesicles*, 2024, **13**, 12397.
39 G. Midekessa, K. Godakumara, J. Ord, J. Viil, F. Lättekivi, K. Dissanayake, S. Kopanchuk, A. Rinken, A. Andronowska, S. Bhattacharjee, T. Rinken and A. Fazeli, *ACS Omega*, 2020, **5**, 16701.
40 V. Krušić Alić, M. Malenica, M. Biberić, S. Zrna, L. Valenčić, A. Šuput, L. Kalagac Fabris, K. Wechtersbach, N. Kojc, M. Kurtjak, N. Kučić and K. Grabušić, *Biomedicines*, 2022, **10**, 785.
41 T. Baranyai, K. Herczeg, Z. Onódi, I. Voszka, K. Módos, N. Marton, G. Nagy, I. Mäger, M. J. Wood, S. El Andaloussi, Z. Pálinkás, V. Kumar, P. Nagy, Á. Kittel, E. I. Buzás, P. Ferdinandy and Z. Giricz, *PLoS One*, 2015, **10**, e0145686.
42 E. A. Mol, M.-J. Goumans, P. A. Doevendans, J. P. G. Sluijter and P. Vader, *Nanomed. Nanotechnol. Biol. Med.*, 2017, **13**, 2061–2065.
43 C. Hsueh, H. Chen, J. K. Gimzewski, J. Reed and T. M. Abdel-Fattah, *ACS Appl. Mater. Interfaces*, 2010, **2**, 3249.
44 Q. Lu, J. Wang, A. Faghihnejad, H. Zeng and Y. Liu, *Soft Matter*, 2011, **7**, 9366–9379.
45 Z. Nurul Sabihah, A. A. Azlan, Z. Nor Dyana, Functionalization Of Mica Surface Using Poly-L-Lysine (Pll) in *Multidisciplinary Research as Agent of Change for Industrial Revolution 4.0*, ed. N. Baba Rahim, European Proceedings of Social and Behavioural Sciences, European Publisher, 2020, vol. 81 pp. 677–682DOI: **10.15405/epsbs.2020.03.03.79**.
46 H. Wang, R. Bash, J. G. Yodh, G. L. Hager, D. Lohr and S. M. Lindsay, *Biophys. J.*, 2002, **83**, 3619–3625.
47 B. Akpinar, P. J. Haynes, N. A. W. Bell, K. Brunner, A. L. B. Pyne and B. W. Hoogenboom, *Nanoscale*, 2019, **11**, 20072–20080.
48 M. Bolean, I. A. Borin, A. M. S. Simão, M. Bottini, L. A. Bagatolli, M. F. Hoylaerts, J. L. Millán and P. Ciancaglini, *Biochim. Biophys. Acta, Biomembr.*, 2017, **1859**, 1911–1920.
49 Y. Chao and T. Zhang, *Appl. Microbiol. Biotechnol.*, 2011, **92**, 381–392.
50 P. Parisse, I. Rago, L. Ulloa Severino, F. Perissinotto, E. Ambrosetti, P. Paoletti, M. Ricci, A. P. Beltrami, D. Cesselli and L. Casalis, *Eur. Biophys. J.*, 2017, **46**, 813–820.
51 R. Rauti, N. Lozano, V. León, D. Scaini, M. Musto, I. Rago, F. P. Ulloa Severino, A. Fabbro, L. Casalis, E. Vázquez, K. Kostarelos, M. Prato and L. Ballerini, *ACS Nano*, 2016, **10**, 4459–4471.
52 J. A. Kiernan, *Microsc. Today*, 2000, **8**, 8–13.
53 Ł. Syga, D. Spakman, C. M. Punter and B. Poolman, *Sci. Rep.*, 2018, **8**, 13789.
54 Y. Feng, M. Liu, X. Li, M. Li, X. Xing and L. Liu, *Nano Lett.*, 2023, **23**, 1591–1599.
55 S. Ye, W. Li, H. Wang, L. Zhu, C. Wang and Y. Yang, *Adv. Sci.*, 2021, **8**, 2100825.
56 S. Yokota, H. Kuramochi, K. Okubo, A. Iwaya, S. Tsuchiya and T. Ichiki, *PLoS One*, 2019, **14**, e0224091.
57 Y. Kikuchi, N. Obana, M. Toyofuku, N. Kodera, T. Soma, T. Ando, Y. Fukumori, N. Nomura and A. Taoka, *Nanoscale*, 2020, **12**, 7950–7959.
58 K. S. Kapoor, S. Kong, H. Sugimoto, W. Guo, V. Boominathan, Y.-L. Chen, S. L. Biswal, T. Terlier, K. M. McAndrews and R. Kalluri, *ACS Nano*, 2024, **18**, 11717–11731.
59 I. Azuri, I. Rosenhek-Goldian, N. Regev-Rudzki, G. Fantner and S. R. Cohen, *Beilstein J. Nanotechnol.*, 2021, **12**, 878–901.
60 M. G. Harrington, A. N. Fonteh, E. Oborina, P. Liao, R. P. Cowan, G. McComb, J. N. Chavez, J. Rush, R. G. Biringer and A. F. Hühmer, *Cerebrospinal Fluid Res.*, 2009, **6**, 10.
61 S. Sharma, H. I. Rasool, V. Palanisamy, C. Mathisen, M. Schmidt, D. T. Wong and J. K. Gimzewski, *ACS Nano*, 2010, **4**, 1921–1926.
62 S. Sharma, B. M. Gillespie, V. Palanisamy and J. K. Gimzewski, *Langmuir*, 2011, **27**, 14394–14400.
63 M. Malenica, M. Perčić, V. Tomas, I. Štajduhar and M. Kurtjak, *Dabar, dataset*, Medicinski fakultet, 2024, **https://urn.nsk.hr/urn:nbn:hr:184:359174**.